Ceramics International 47 (2021) 16152–16161

Contents lists available at ScienceDirect

Ceramics International

journal homepage: www.elsevier.com/locate/ceramint

Towards anti-angiogenic activity of $NiFe_2O_4$ nanoparticles

J.G. Santos [a,*], H. Lopes [a], H. Moreno [a], M.A. Ramirez [a], F.G. Garcia [b], A.Z. Simões [a]

[a] São Paulo State University (UNESP), School of Engineering of Guaratinguetá, São Paulo, Guaratinguetá, Brazil
[b] Federal University of Itajubá (UNIFEI), Institute of Physical and Chemistry, Av. BPS, 1303, Itajubá, Minas Gerais, Brazil

ARTICLE INFO

Keywords:
$NiFe_2O_4$
Polymeric precursor method
Surfactant
Anti-angiogenic

ABSTRACT

In this study, $NiFe_2O_4$ nanoparticles (NPs) were prepared using the polymeric precursor method and calcined at 500°C for 4 h with (S– $NiFe_2O_4$) and without ($NiFe_2O_4$) CTAB as a surfactant, respectively. The magnetic and biological properties were evaluated based on the (micro)structure and electronic structure of the NPs. On sample S–$NiFe_2O_4$, the significant increase in magnetization saturation (M_s ~ 61.84 emu/g), magnetic remanence (M_r ~ 4.30 emu/g), and coercivity (H_c ~ 0.475 kOe) in comparison to sample $NiFe_2O_4$ (M_s ~ 24.81 emu/g, M_r ~ 1.00 emu/g, and H_c ~ 0.475 kOe) at room temperature (300 K) may be associated with the presence of oxygen vacancies the spinel lattice of $NiFe_2O_4$, generating magnetic moments. The concentration of 1 μg/mL S–$NiFe_2O_4$ decreased in ~50% angiogenesis in the chorioallantoic membrane (CAM). S–$NiFe_2O_4$ NPs showed high blood vessel affinity and anti-angiogenic activity; hence, effectively concentrating on tumoral vessels, which may enhance drug effectivity and enable simultaneous treatments, image diagnosis of solid tumors, etc. Thus, our results suggest that CTAB addition is an effective way to tune its magnetic response due to its excellent biocompatibility, high bulk saturation magnetization, and low magnetic anisotropy.

1. Introduction

In the last decades, researchers have turned their attention to the iron-based magnetic complex oxides due to their wide range of electromagnetic properties, which enable practical applications in biomedicine [1,2]. As nanomaterials arise as a solution in the biomedical field for drug delivery [3,4], hyperthermia [5–7], tissue repair [8], and cell separation/purification [9,10] the production of engineered nanoparticles (1–100 nm) has increased exponentially in the last few years. In this scenario, it becomes critical to develop a deep understanding **of** the potential risks associated with the nanoparticles' interactions in the human body (e.g., biocompatibility, toxicity, etc.) [11].

Nickel ferrite ($NiFe_2O_4$) exhibits a strong magnetic response due to its intrinsically high magneto-anisotropy ascribed to its spinel structure, making it suitable for various applications, especially in biomedicine [12,13]. Its structure is formed by tetrahedrally coordinated Fe^{3+} ions (A sites), whereas Ni^{2+} and Fe^{3+} ions share the octahedral (B) sites. Hence, nickel ferrite may be represented as $(Fe^{3+})_A[Ni^{2+}Fe^{3+}]_BO^{2-}{}_4$ [14,15]. Its net magnetization originates exclusively from Ni^{2+} spin moments in $Ni(Fe)O_6$ clusters, while the antiparallel Fe^{3+} spin moments in $Ni(Fe)O_4$ and FeO_6 clusters cancel one another [16], generating ferrimagnetic's response, which is significantly influenced by the NPs' (micro)structure and composition [17]. Thus, it is necessary to use a well-controlled preparation route to synthesize the NPs [18,19]. The magnetic properties of ferrites are also strongly affected by the dopant (type, size, etc.) and method of synthesis. Several researchers have addressed rare-earth doping due to their large size, which enhances the magneto-anisotropy associated with the ferrite spinel crystal as a result of the 3d–4f spin coupling [14,20–22]. On the other hand, different preparation methods have been employed to obtain nickel ferrite NPs [23], including the sol-gel method [16,24,25], hydrothermal [26–28], microwave-assisted methods [29,30], combustion method [15,31], and polymeric precursor method (PPM) [32,33]. PPM stands out compared to conventional solid-state reaction method for enabling the synthesis of high-crystallinity NPs through a well-controlled thermal treatment, at lower processing temperatures, with better stoichiometry control, homogeneity, and purity [34–37]. Surfactants (e.g., Cetyl trimethyl ammonium bromide - CTAB, $[(C_{16}H_{33})N(CH_3)_3]Br$) affect particle shape and size. Dinkar et al. [28] used CTAB to improve control over the shape and size of $NiFe_2O_4$ NPs. The use of a surfactant may also help decrease NP agglomeration, which is common in magnetic materials [21]. Apart from controlling the size, CTAB also plays a key role in decreasing surface tension in the solution, which reduces the energy required for crystallization [38]. CTAB also proved effective as an antiseptic agent

* Corresponding author.
E-mail address: jonathas.gabriel@unesp.br (J.G. Santos).

https://doi.org/10.1016/j.ceramint.2021.02.191
Received 18 October 2020; Received in revised form 13 January 2021; Accepted 21 February 2021
Available online 24 February 2021

against bacteria and fungi, having been widely used to synthesize gold NPs (e.g., spheres, rods, bipyramids, etc.), mesoporous silica NPs (e.g., MCM-41), and hair conditioning products [39,40]. Liver cancer or hepatocellular carcinoma (HCC) is responsible for countless deaths worldwide, second only to heart and infectious diseases. Hence, nanoparticles' (NPs) (e.g., nickel ferrite – $NiFe_2O_4$) are receiving more attention from researchers for enhancing radio/chemotherapy effectiveness as well as in hyperthermia due to its anti-angiogenic activity associated with its noninvasive nature and cell-selective mechanism. Based on the strong magnetic response of nickel ferrite and the possibility to further improve its magnetic properties using CTAB as a surfactant for synthesizing S–$NiFe_2O_4$ NPs using the polymeric precursor method, in this work we evaluate its biological response envisioning future bimedical applications. The use of magnetic NPs appear very beneficial due to remarkable heating effects (hyperthermia), enabling tumor specific cell-targeting and controlled-release drug delivery mechanisms. The possibility to replace/enhance the effect of traditional drugs used in chemo-/radiotherapy is exciting since it considerably reduces the side effects associated with cancer treatment. Hence, understanding the biological response of $NiFe_2O_4$ NPs and its toxicity becomes critical. Tumoral expansion and metastasis depends on angiogenesis, or blood vessel formation. Hence, the development of new methods/materials capable of blocking neovascularization around solid tumors contributes significantly to the effectiveness of antitumor therapy, as suggested by Folkman et al. [41] since 1980. The $NiFe_2O_4$ NPs showed high affinity with the tumor tissue.

In this study, spinel $NiFe_2O_4$ NPs were synthesized via the polymeric precursor method in two different solutions: (1) without surfactant - $NiFe_2O_4$ and; (2) with surfactant (CTAB) - S–$NiFe_2O_4$. The (micro) structure and magnetic response of the NPs were correlated for evaluating the effect of CTAB on the magnetic response of $NiFe_2O_4$ NPs. Our results suggest the possibility to tune the magnetic response of $NiFe_2O_4$ NPs by using CTAB, making S–$NiFe_2O_4$ NPs a promising substitute to iron oxides (Fe_3O_4 or γ-Fe_2O_3) with excellent biocompatibility (no cytotoxic effect), high bulk saturation magnetization, and low magnetic anisotropy. To the best of our knowledge, there are no reports on the anti-angiogenesis properties of spinel $NiFe_2O_4$ NPs.

2. Experimental procedure

2.1. Synthesis

Nickel Ferrite ($NiFe_2O_4$) was synthesized using the polymeric precursor method [47,48]. First, precursor solutions of Fe^{3+} and Ni^{2+} were prepared separately by adding ammonium iron (III) citrate ($C_6H_{11}FeNO_7$: 98.1%; Mallinckrodt) and nickel nitrate hexahydrate ($Ni(NO_3)_2.6H_2O$: 97.0%; Alfa Aesar) to ethylene glycol ($C_2H_6O_2$: 99.7%; Synth) and concentrate citric acid monohydrate ($C_6H_8O_7.H_2O$: 99.5%, Merck) at a molar ratio of 1:4:16 (metal: citric acid: ethylene glycol) under constant heating and stirring. The Fe^{3+} and Ni^{2+} solutions were combined and constantly stirred for 2 h at 90°C for homogenization. Then, the temperature was increased to 130–140°C to obtain **a** high-viscosity polyester resin. The yield resin was separated into two aliquots. To the first part, CTAB ($((C_{16}H_{33})N(CH_3)_3]Br$, 98.0%, Nuclear) – concentration ~ 5 μg/mL - was added as surfactant. Part of the polymer resin without surfactant was combusted at 300 °C for 2 h for evaluating its decomposition and crystallization characteristics/temperatures. Finally, two samples in the form of powders were obtained calcining the polyester resins without ($NiFe_2O_4$) and with surfactant (S–$NiFe_2O_4$) under air atmosphere in a furnace at 500 °C for 4 h at a heating rate of 10°C/min, as determined by thermogravimetric analysis (TG-DTG) (Fig. S1).

3. Characterizations

3.1. (Micro)structural characterization

X-ray Powder diffraction XRPD was performed on the samples on a Rigaku diffractometer (model D/Max-2400) using the *Cu-K*$_\alpha$ radiation (λ ~1.54 Å) in the range $20° \leq 2\theta \leq 80°$ (step size ~ 0.02°). Phase identification was carried out based on the Inorganic Crystal Structure Database (ICSD), and the crystal structure of the powders was refined using the Rietveld method [42] on Topas V.5 in its academic version [43]. All the lattice parameters were refined using a 3rd order Chebychev polynomial, and the statistical parameters associated with the crystalline structure (R_{Bragg}, R_{wp}, R_{exp} and χ^2) were estimated. Fourier transform - Infrared spectra were collected on a Bruker spectrophotometer (model EQUINOX/55) over the range of 500–4000 cm^{-1} (step ~ 1.9 cm^{-1}) to detect possible contaminants from the precursor reagents. Raman spectroscopy was performed on a Bruker spectrometer (model RFS-100/S) using **a** 1064 nm Yttrium Aluminum Garnet (YAG) laser as the excitation source (150 mW), from 100 to 800 cm^{-1} (step ~ 1.9 cm^{-1}) coupled to a CCD detector. Powder microstructure was investigated using a field emission gun coupled scanning electron microscopy (FEG-SEM) on a Supra (model 35-VP, Carl Zeiss, Germany) operating at 5.00 kV. The average particle size was measured using the freeware NIH ImageJ [44,45]. Transmission electron microscopy (TEM) and energy dispersive spectroscopy (EDS) analysis were carried out on an FEI microscope (model Tecnai G2 F20, USA) operating at 200 kV and 15 kV, respectively.

3.2. Optical response

Ultraviolet–visible (UV–vis) spectroscopy was performed on a Varian spectrophotometer (model Cary 5G, USA) in diffuse reflectance mode. The optical bandgap energy (E_{gap}) was graphically determined based on the Kubelka-Munk equation (Eq. (1)):

$$\alpha h\nu = C_1\left(R_\infty\left(h\nu - E_{gap}\right)^n\right) \quad (1)$$

where α is the linear absorption coefficient, h Planck's constant ($h = 4.1357 \times 10^{-15}$ eV s^{-1}), ν the frequency of the light, C_1 is a constant, and R_∞ is the reflectance for an infinitely thick sample. Note that n can assume specific values depending on the electronic transition (n = 1/2, 3/2, 2 or 3 for direct allowed, indirect forbidden, direct forbidden, and indirect forbidden, respectively) [46]. The best linear fit obtained for the $(\alpha h\nu)^2$ vs. Energy ($h\nu$) plots (Tauc plots) were used to estimate the optical bandgap energy of the samples.

3.3. Magnetic response

The magnetic measurements were carried out in the Vibrating Sample Magnetometer (VSM) (model Quantum Design PPMS DynaCool) at four different temperatures for each sample (5, 200, 300, and 390 K) exposed to a dc magnetic field up to ±30 kOe. Zero-field cooled (ZFC) plots were obtained cooling the samples without applying a magnetic field. Analogously, to obtain the field cooled (FC) plots the samples were cooled from room temperature to temperatures close to zero while a 0.005 T magnetic field was applied. The magnetization was measured as a function of temperature.

3.4. Biological response

The S–$NiFe_2O_4$ sample was tested against the anti-angiogenic activity in a chicken embryo chorioallantoic membrane (CAM) in the biological medium and NaCl solution (0.9%). Silanization is a two-stage process. First, an ethanol solution of the organosilane is added to an acidic medium, acting as a catalyst. Then, a combination of hydrolysis and condensation reactions form a silane polymer. In the hydrolysis

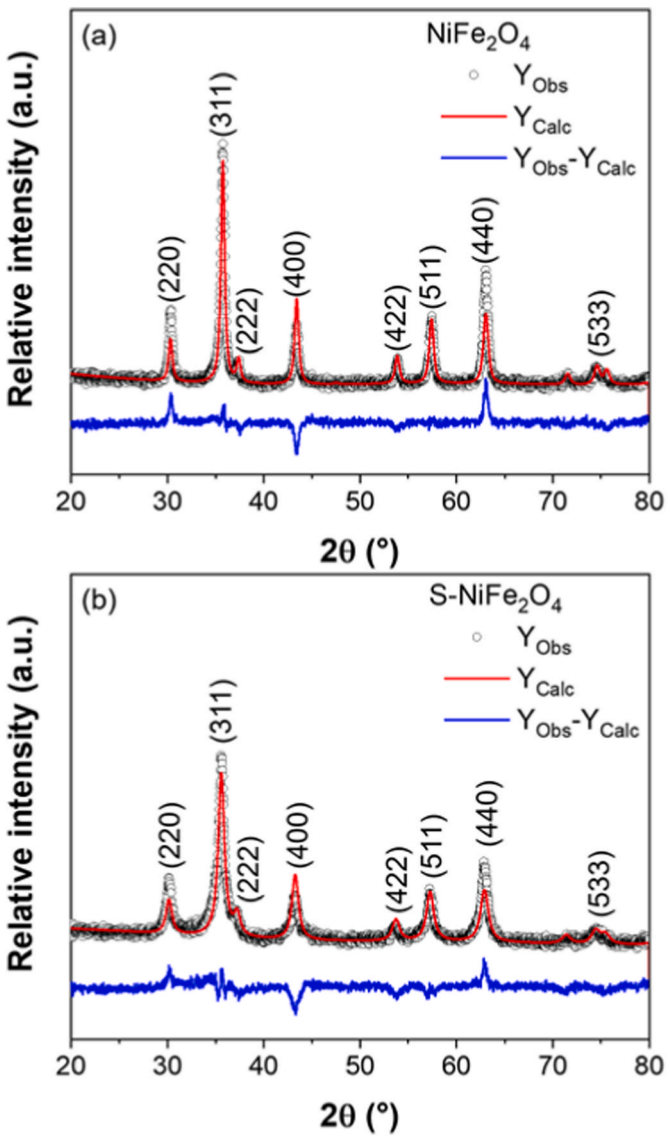

Fig. 1. XRPD patterns and Rietveld refinement for samples (a) $NiFe_2O_4$ and (b) S–$NiFe_2O_4$ obtained at room temperature. The inset (c) shows $NiFe_2O_4$ (311) peak displacement/broadening.

reaction, alkoxide groups (O–CH_3) are replaced by the hydroxyl group, OH, to form the silanol group (H_3Si–OH), which condenses with other silanol groups to produce siloxane (Si–O–Si) bonds. Methanol and water are produced as by-products of condensation. Polymer-nanoparticle association occurs in the second stage through covalent bonding due to the presence of OH groups. Polymer adsorption on the surface of NPs occurs through dehydration. 2-hydroxyethyl methacrylate monomer (HEMA, Aldrich) was used as received. The concentration of ammonium persulfate (PSA, ~0,05%) and tetramethyl ethylenediamine (TEMED, ~0,015%) were based on the total number of moles of HEMA monomer. TEMED reduces PSA half-life by accelerating the formation of free radicals and, hence, the HEMA polymerization reaction. Methyl-ethyl-ketone (MEK) and cyclohexane (CH) were used as a solvent and a non-solvent, respectively. Gelatin (1 wt%) and NaCl (2 wt%) were used as suspending agents to promote the "salting out" effect. To obtain the aqueous phase (AP), an S–$NiFe_2O_4$ suspension was dissolved in a sodium chloride solution ($NaCl_{(aq)}$) at 4°C, mechanically stirred (~800 rpm). Analogously, to obtain the organic phase (OP), PSA was dissolved in HEMA at room temperature. The OP was pre-polymerized at 50 °C for 30 min under mild magnetic stirring and, then added to the diluent mixture, MEK/CH, and homogenized. The organic phase was added to the aqueous phase at a 5: 1 ratio (v: v) under constant stirring for 20 min. Then, the mixture was heated to 30°C for 24 h and constantly stirred at 800 rpm. To assess the anti-angiogenic activity of the samples, *Gallus domesticus* (Ross lineage) embryonic eggs were incubated at 37°C and 60% relative humidity horizontally on an automatic digital incubator (Premium Ecological®). On the third day of embryonic development, a 2.0 cm circular incision was made in the eggshell air chamber. Non-embryonic eggs were discarded. The inner eggshell membrane was removed, exposing the chick embryo chorioallantoic membrane (CAM). Then, the eggs were sealed with transparent adhesive tape. The eggs were placed on a vertical styrofoam support inside the incubator, where they remained for two more days, until the fifth day of embryonic development. The dose-response curve was obtained inoculating 20 μL of a suspension containing S–$NiFe_2O_4$ nanoparticles (NPs) in standard cellulose discs previously placed on the CAM. Inoculations were performed on the fifth and sixth days of embryonic development. The experiment was divided into four experimental groups, varying NPs concentrations: (1) Sterile physiological saline (0.9% w/V) – negative control; (2) NPs (1.00 μg/mL); (3) NPs (10.0 μg/mL; and (4) NPs (20.0 μg/mL). On the seventh day of embryonic development, 48 h after the first NP suspension inoculation, the CAMs were extracted with a 3.7% formaldehyde solution for 10 min. The results were subjected to analysis of variance (ANOVA) followed by post-test Bonferroni or Newman-Keuls for multiple comparisons. The statistical analyzes were performed using the Graphpad Prism 5.0 software to Windows (Graphpad Software Inc., California, USA). The data were expressed as average ± standard deviation (SD), and the level of significance established was $p < 0.05$. A digital camera (Leica Application Suite V 3.3.0, Germany) coupled to a stereomicroscope (Leica, model DM4000B, Germany) was used to record the images. The freeware NIH Image J was used to analyze the blood vessels in the images. The saline solution [NaCl 0.9% w/V (negative control)] results were fixed as 100% for calculating blood vessels' reduction (in %). The anti-angiogenic activity was evaluated in the S–$NiFe_2O_4$ NPs, which exhibited lower agglomeration and smaller NPs (particle size ~ 28.64 ± 6.51 nm) in comparison to the $NiFe_2O_4$ sample.

4. Results and discussion

4.1. (Micro)structural characterization

Fig. 1(a and b) displays the XRPD patterns for the samples synthesized without ($NiFe_2O_4$) and with surfactant (S–$NiFe_2O_4$) treated using the Rietveld method. In both samples, all diffraction peaks are associated with the $NiFe_2O_4$ phase (ICSD #28108) with a spinel structure and *Fd-3mS* space group [47]. No secondary phase peaks were identified. The geometric and Rietveld parameters obtained for the samples are

Table 1
Rietveld Refinement data of $NiFe_2O_4$ powders crystallized in a conventional furnace in static air at 500 °C for 4 h in static air in the presence and absence of CTAB as a surfactant.

Sample	Geometric parameters						Rietveld parameters			
	Strain	Crystallite size (nm)	a = b = c (Å)	V (Å^3)	phase %	R_{Bragg}	R_{exp}	R_{wp}	R_p	χ^2
$NiFe_2O_4$	0.026	24.7	8.34	580.2	100.0	7.658	6.54	7.88	5.63	1.21
S–$NiFe_2O_4$	0.269	14.5	8.35	581.4	100.0	10.35	5.96	7.19	5.45	1.21

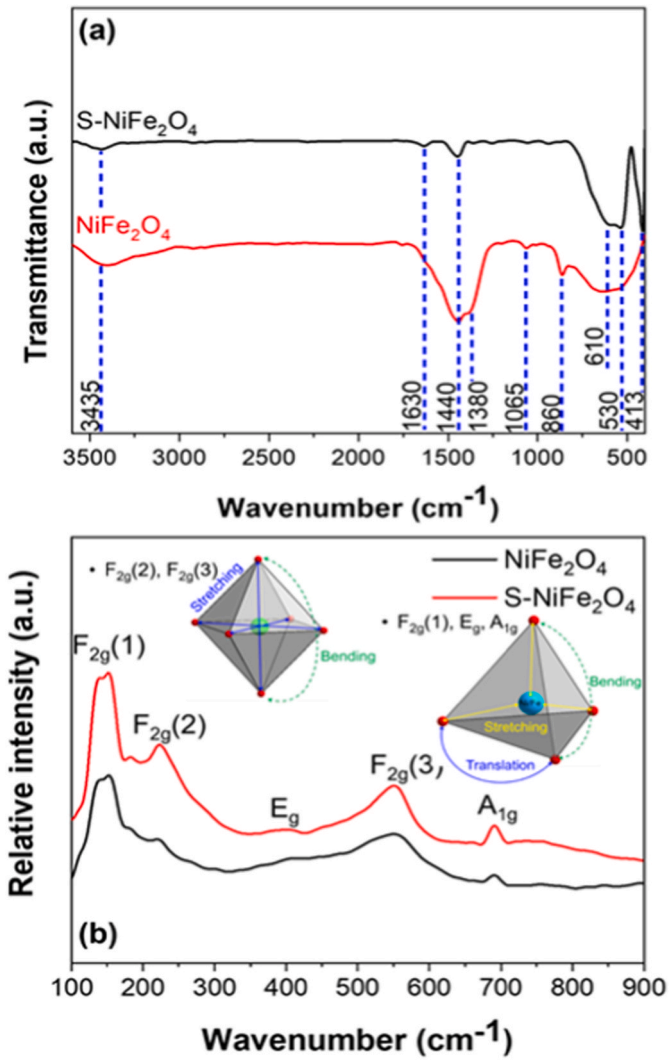

Fig. 2. (a) FT-IR and (b) Raman spectra for samples $NiFe_2O_4$ and S–$NiFe_2O_4$ obtained at room temperature.

shown in Table 1. The Rietveld parameters (R_{exp}, R_{wp}, R_p, and χ^2) indicate a coherent fitting of the XRD data [48–50]. Sepelak et al. [51] associated the intensity ratio of peaks (220) to (222) with Ni/Fe site inversion in spinel structures. An inverse spinel structure is characterized by Fe^{3+} occupying the tetrahedral A site and Ni^{2+} ions occupying the octahedral B sites. Thus, peaks (220) and (222) represent sites A and B contributions alone, whose structure factor is defined by Eqs. (2) and (3):

$$|F_{220}|^2 = 2\left(f_A + 4f_O\cos^2 4\pi u\right)^2 \quad (2)$$

$$|F_{222}|^2 = 8\left(f_B + 2f_O\sin^3 4\pi u\right)^2 \quad (3)$$

where f_A, f_B, and f_O are the atomic structure factors of sites A, B, and oxygen, respectively, and u indicates the lattice's oxygen positions. While Ni/Fe site inversion does not affect peaks (220) and (222) relative intensity, oxygen coordinate changes (u) have a significant effect on it. The XRD results show that on S–$NiFe_2O_4$ NPs, the disorder is induced by site inversion generating a strained, contracted lattice compared to the $NiFe_2O_4$ NPs. The percentage of iron ions in site B increases with grain size reduction. Rietveld analysis shows minor changes related to Ni/Fe site inversion. However, the intensity of peaks (220) and (222) decreases significantly, which can be associated with oxygen coordinate changes [52,53].

Table 2
Structural data of $NiFe_2O_4$ powders crystallized in a conventional furnace in static air at 500 °C for 4 h in static air in the presence and absence of CTAB as a surfactant.

		Motion description	Observed wavenumber (cm^{-1})
FTIR		Fe–O stretching in FeO_6 octahedra	413 530
		Ni/Fe—O stretching in Ni(Fe)O_4 tetrahedra	610
		CO^{3-}	860
		C—O stretching vibrations	1065
		CO—H vibrations	1380 1440
		OH bending vibrations of H_2O	1630
		OH stretching vibrations of H_2O	3435
	Mode	Motion description	Observed wavenumber (cm^{-1})
Raman	$F_{2g}(1)$	Ni/Fe—O translation in Ni(Fe)O_4 tetrahedra	151
	$F_{2g}(2)$	Fe—O asymmetric stretching in FeO_6 octahedra	224
	E_g	Ni/Fe—O symmetric bending in Ni(Fe)O_4 tetrahedra	390
	$F_{2g}(3)$	Fe—O bending in FeO_6 octahedra	551
	A_{1g}	Ni/Fe—O symmetric stretching in Ni(Fe)O_4 tetrahedra	691

Additionally, sample S–$NiFe_2O_4$ (d_{311} = 14.5 nm) presented smaller crystallites compared to $NiFe_2O_4$ (d_{311} = 24.7 nm). This effect suggests the formation of a reverse spinel structure, in which crystallite size reduction occurs as a result of nickel ions moving from site B to site A, while an equal amount of iron ions move from site A to B, which becomes more significant as particle size decreases [53]. Hence, crystallite size reduction may be associated with higher structural strain in the nanoparticles synthesized with the presence of a surfactant (CTAB), observed in the form of a slight peak shift/broadening. Fig. 1 (c) shows that the peak related to the plane (311) shifts towards smaller Bragg angles, indicating the occurrence of uniform strain in the S–$NiFe_2O_4$ lattice in comparison to $NiFe_2O_4$ NPs. Additionally, peak (311) also becomes broader, suggesting non-uniform lattice strain, causing lattice contraction.

Fig. 2(a) displays the FT-IR spectra obtained for the $NiFe_2O_4$ and S–$NiFe_2O_4$ samples. Two main absorption bands below 1000 cm^{-1} are common to all spinel ferrite structures. The band at ~413 cm^{-1} may be ascribed to the stretching vibration of $Fe^{3+} - O^{2-}$ bonds in the Ni(Fe)O_6 octahedra. 610-530 cm^{-1} band is related to the intrinsic vibrational stretching mode of $Fe^{3+} - O^{2-}$ bonds in the Ni(Fe)O_6 octahedra [29,54]. The difference in absorption frequency for octahedral and tetrahedral clusters in the $NiFe_2O_4$ crystals results from bond length differences for the $Fe^{3+} - O^{2-}$ bonds in octahedral and tetrahedral sites [54]. The intensities of the absorption bands are found to increase for sample S–$NiFe_2O_4$ compared to $NiFe_2O_4$, suggesting that the use of CTAB increases ferrite's structural order. Vibrational bands at 1065/860 cm^{-1} and 1380/1440 cm^{-1} may be associated with carbonates (CO^{3-}) and CO–H bending vibrations in the carbon chains, respectively [55]. Finally, absorption bands at 1630 and 3435 cm^{-1} are related to bending and stretching vibration of OH bonds of free/absorbed water molecules [27]. At 1440, 1065, and 860 cm^{-1}, the bands practically disappear in the S–$NiFe_2O_4$ sample, indicating the formation of pure spinel structure $NiFe_2O_4$ without CTAB contaminants. Table 2 summarizes each bands' absorption frequency and vibrational mode associated. Fig. 2 (b) shows the Raman spectra collected at room temperature for samples $NiFe_2O_4$ and S–$NiFe_2O_4$. According to the group theory, there are 16 vibrational groups possible for $NiFe_2O_4$: A_{1g}, E_g, F_{1g}, 3 F_{2g}, 2 A_{2u}, 2 E_u, 4 F_{1u}, 2 F_{2u}, of which five (A_{1g} + E_g + 3 T_{2g}) are Raman active [50,56,57]. All $NiFe_2O_4$ vibrational modes show a shoulder-like feature at the lower wavenumber, indicating a doublet-like feature [57]. The broad modes

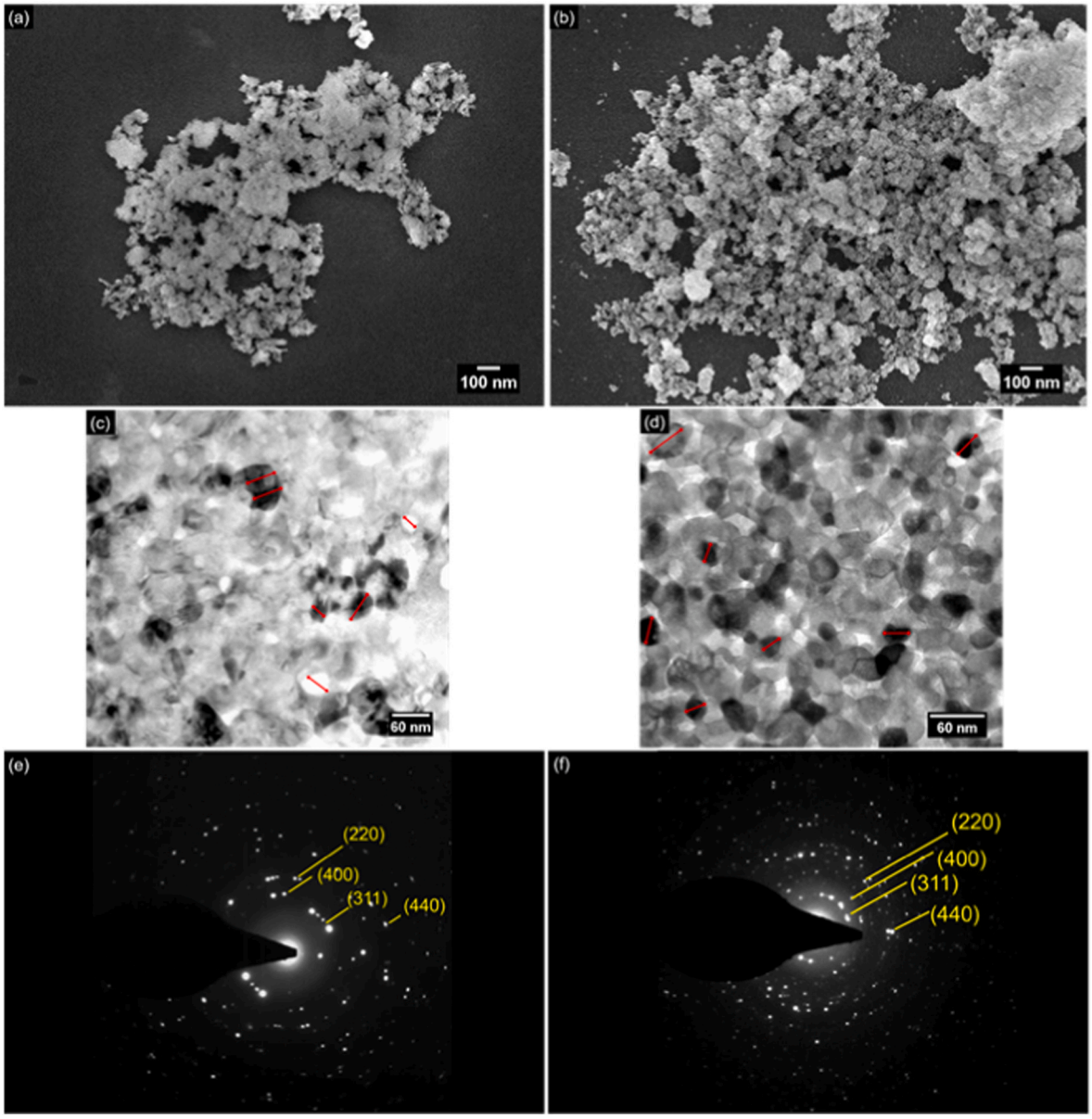

Fig. 3. (a) $NiFe_2O_4$ and (b) S–$NiFe_2O_4$ FE-SEM; (c) $NiFe_2O_4$ and (b) S–$NiFe_2O_4$ HRTEM. (the red lines show the NPs measured in imageJ for determining the average particle size); and (e) $NiFe_2O_4$ and (f) S–$NiFe_2O_4$ SAED micrograph images for the samples calcined in a conventional furnace under a static air atmosphere at 500 °C for 4 h. (For interpretation of the references to colour in this figure legend, the reader is referred to the Web version of this article.)

suggest low short-range order. At 224 and 551 cm^{-1}, modes $F_{2g}(2)$ and $F_{2g}(3)$ are associated with Fe–O asymmetric stretching and bending in the $Ni(Fe)O_6$ octahedra, respectively. Vibrational modes $F_{2g}(1)$, E_g, and A_g (at 151, 390, and 691 cm^{-1}) may be ascribed to translation, symmetric bending, and symmetric stretching of Ni/Fe—O bonds in FeO_4 tetrahedra [50,58]. On S–$NiFe_2O_4$ samples, the peak-shift towards higher wavenumbers for all vibrational modes indicates lattice expansion, corroborating the Rietveld analysis. Table 2 summarizes each modes' wavenumber and vibrational motion associated.

Fig. 3(a and b) displays micrograph images of both samples. On sample S–$NiFe_2O_4$, the surfactant causes the dispersion of the agglomerated particles, which may strongly affect its magnetic response. Higher dispersion decreases the anisotropy characteristic of nickel ferrite systems, favoring the physical properties' homogeneity in different directions. In the sample crystallized in the presence of CTAB, the higher dispersion of the NPs may favor the effect of an external magnetic field, improving the system's magnetic response. The micrograph image of sample $NiFe_2O_4$ (Fig. 3a) shows highly agglomerated NPs (average particle size ~ 36.75 nm). Particles with nanometric dimensions tend to agglomerate due to lower surface energy associated with this spatial configuration and as a result of the van der Waals forces caused by the nucleation process at higher *OH-* concentration with no separation of particles. CTAB plays a key role in particle nucleation and growth kinetics by reducing the surface tension in the solution during the synthesis of nickel ferrite. Hence, the system needs a smaller amount of energy to crystallize, reducing the particle size. Fig. 3(c and d) displays TEM micrograph images for a clearer view of the size, morphology, and crystallinity of the prepared NPs at high resolution. The micrograph images show highly agglomerated NPs of irregular morphologies, which drastically change with CTAB addition. Agglomeration may be ascribed both to the particles' magnetic nature and to the surface energy minimization effects associated with NPs. The particles have some size distribution as judged by the individual particles (see red arrows in Fig. 3c and d), suggesting that the particle size is smaller than 50 nm.

Besides morphology changes, the addition of CTAB to the PPM solution leads to the formation of slightly smaller NPs - $NiFe_2O_4$ (particle

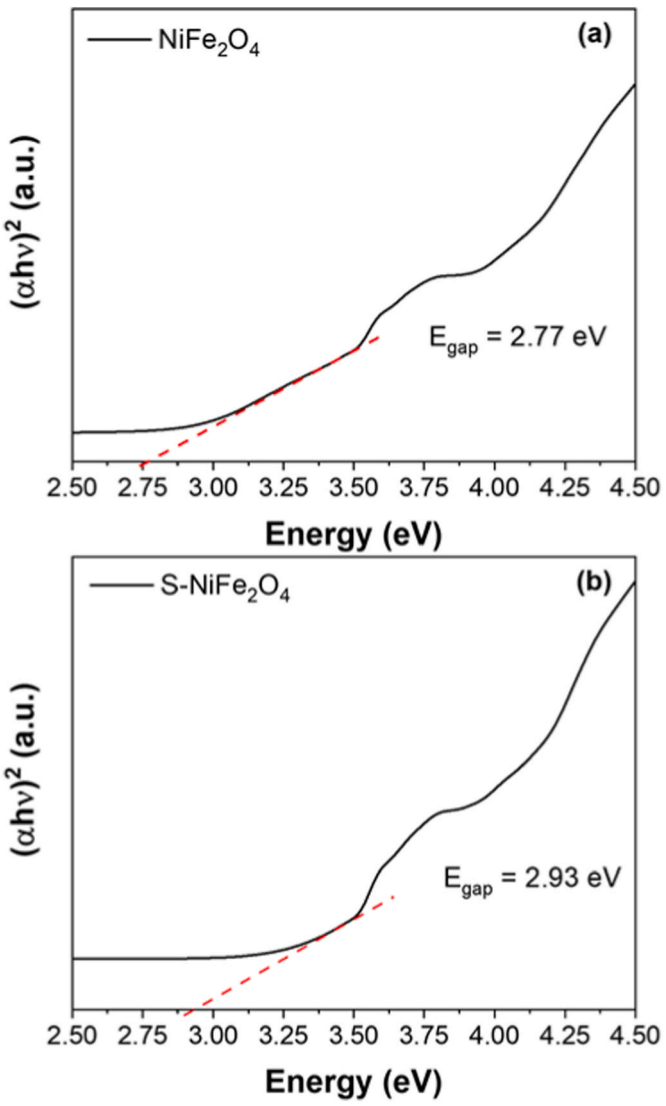

Fig. 4. Tauc plots for samples (a) $NiFe_2O_4$ and (b) S–$NiFe_2O_4$, calcined in a conventional furnace under a static air atmosphere at 500 °C for 4 h.

size ~ 36.75 ± 10.76 nm) and S–$NiFe_2O_4$ (particle size ~ 28.64 ± 6.51 nm). Smaller S–$NiFe_2O_4$ NPs appear less agglomerated in the powder, corroborating to FE-SEM analysis (Fig. 3a and b), which may be an effect associated with CTAB. Furthermore, one can observe better-defined particle contours on sample S–$NiFe_2O_4$, indicating that the surfactant significantly affects particle morphology and crystallinity in the nickel ferrite systems. Hence, it may be possible to develop synthetic routes for morphological control. *SAED* images (Fig. 3e and f) indicate highly crystalline samples with well-defined lattice fringes. The position/intensity of the lines in the SAED pattern suggests polycrystalline nanoparticles' samples, confirming a high purity single-phase $NiFe_2O_4$ spinel structure, corroborating the Rietveld analysis. The spacing between neighboring lattice fringes was measured and linking to the corresponding plane using ICSD card number 86–2267.

4.2. Optical response

Fig. 4(a and b) presents the ultraviolet–visible (UV–Vis) spectra collected at room temperature in diffuse reflectance mode for the $NiFe_2O_4$ nanoparticles. The Kubelka-Munk mathematical model (Eq. (1)) was applied to obtain the $(\alpha h\nu)^2$ vs. Energy curves. Both samples behaved as expected for the nickel ferrite system with a spinel structure, $NiFe_2O_4$ (E_{gap} ~ 2.77 eV), and S–$NiFe_2O_4$ (E_{gap} ~ 2.93 eV) [59]. For a perfect crystal of $NiFe_2O_4$, it was expected to observe a well-defined absorption curve and, thus, an E_g value of ~2.7 eV; however, the density of defects present in the NPs promotes a reduction in E_g. The S–$NiFe_2O_4$ showed the highest bandgap energy. This value is justified by the higher structural strain in the NPs synthesized with the presence of a surfactant (CTAB), which can be observed in the form of slight peak shift/broadening. Therefore, the crystallization of $NiFe_2O_4$ based materials with CTAB changed the average size of nanocrystals. The surfactant's chemical nature (polarity, dielectric properties, solubility) interacts differently with the dissolved ions, influencing crystals' crystallization, and growth processes. Therefore, these tails indicate that there are electronic levels located within the prohibited band, which are associated with defects such as distortions and vacancies that cause a structural lattice disorder, as previously observed in XRPD measurements. Such energy gap value is associated with electronic transitions between oxygen 2p with d orbitals of Ni and Fe elements. The different energy levels are governed by the orbital overlapping of d and p orbital projected in $NiFe_2O_4$-based material near the Fermi level, generating electron transitions from the valence to the conduction band. Hence, both $NiFe_2O_4$ samples showed medium-range disorder behavior.

4.3. Magnetic response

Fig. 5(a) shows room temperature (300 K) hysteresis loops for samples $NiFe_2O_4$ and S–$NiFe_2O_4$. $NiFe_2O_4$ NPs displayed lower magnetization saturation (M_s) in comparison to S–$NiFe_2O_4$, 24.81, and 61.84 emu/g, respectively. Additionally, sample S–$NiFe_2O_4$ presents higher magnetization remanence (M_r ~ 4.30 emu/g) and coercivity (H_c ~ 0.475 kOe) (see the inset in Fig. 5a) in accordance with the released literature [60]. This behavior may be associated with oxygen vacancies in spinel structured $NiFe_2O_4$, leading to the formation of magnetic moments. Therefore, the different magnetic responses may be associated with spin moments from [Ni/FeO_6] octahedral and [FeO_4] tetrahedral clusters in the disordered $NiFe_2O_4$ lattice, which significantly affect the exchange coupling and magnetic properties of the as-prepared NPs.

The Rietveld analysis suggests a reverse spinel structure is formed in the S–$NiFe_2O_4$ samples, which may explain smaller crystallites compared to $NiFe_2O_4$ samples. For NPs with a spin-glass-like surface layer and ferrimagnetically lined-up core spins become smaller, the surface layer spins' disorder generates a higher associated M_s. The spin-glass (SG) effect is more prominent in the S–$NiFe_2O_4$ NPs due to the strain generated by site inversion compared to $NiFe_2O_4$ NPs. The SG effect in oxides is generally associated with oxygen vacancies and produces broken bonds [61]. These free-radicals induce spin disorder, generating randomness in exchange interactions. Oxygen vacancies promote cationic redistribution within the lattice. Additionally, the CTAB restores the electron state density and crystalline field on the surface of nanocrystals for those atoms near the surface layer, affecting spin moments of [Ni/FeO_6] octahedral and [FeO_4] tetrahedral clusters in the disordered $NiFe_2O_4$ lattice [62]. Therefore, our results suggest that oxygen vacancies generated by CTAB addition may be the main reason for the SG effect, influencing the NPs' magnetic response and, hence, surface adhesion.

A multidomain magnetic structure may arise on sample $NiFe_2O_4$ due to significant particle agglomeration, which leads to a mean particle size larger than the single critical domain. It may also be argued that the increase in M_s, M_r, and H_c may be due to changes associated with the materials' domain structure (e.g., critical diameter, crystal anisotropy, etc.), which may result from particle size decrease [14,49,63,64], as indicated in the microstructural analysis. On sample $NiFe_2O_4$, a weaker magnetic response may be ascribed to its higher degree of agglomeration, increasing average particle size distribution (36.75 ± 10.76 nm) and generating larger domains, which play a key role in a multidomain magnetic structure such as nickel ferrite. It is well established that the presence of oxygen vacancies in spinel structure $NiFe_2O_4$ can generate

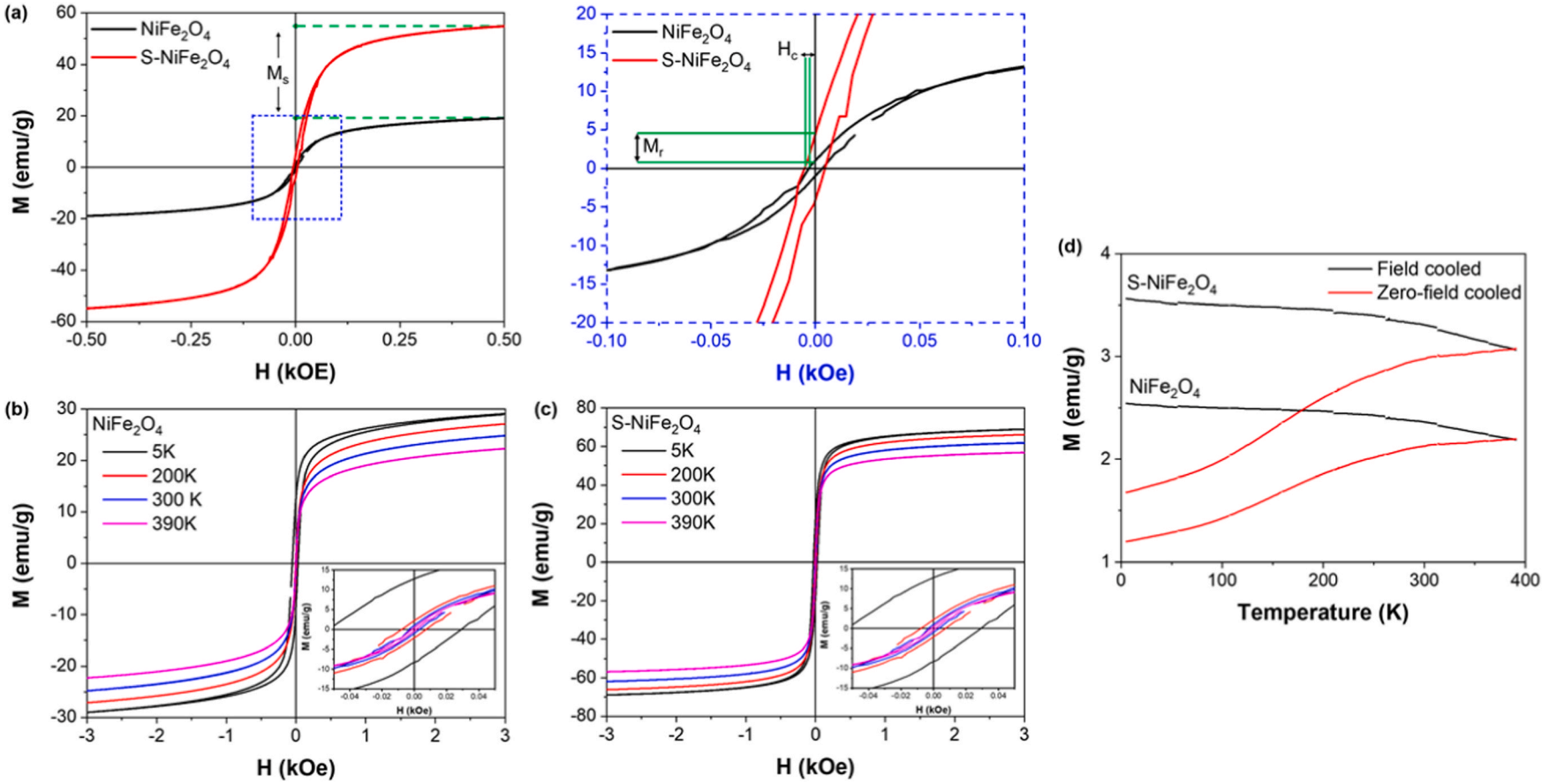

Fig. 5. Hysteresis loops for samples $NiFe_2O_4$ and S–$NiFe_2O_4$ obtained at (a) 300 K, and at different temperatures (5–390 K) for samples (b) $NiFe_2O_4$ and (c) $NiFe_2O_4$. (d) Zero-field cooled (ZFC) and field cooled (FC) plots for samples $NiFe_2O_4$ and S–$NiFe_2O_4$ obtained for an applied magnetic field of 0.005 T.

Table 3
Magnetic parameters of $NiFe_2O_4$ powders crystallized in a conventional furnace in static air at 500 °C for 4 h in static air in the presence and absence of CTAB as a surfactant.

Sample	Temperature (K)	H_c (kOe)	M_r (emu/g)	M_s (emu/g)
$NiFe_2O_4$	5	4.150	10.54	29.03
	200	0.768	2.17	27.11
	300	0.318	1.00	24.81
	390	0.130	0.40	22.26
S–$NiFe_2O_4$	5	2.815	21.06	68.93
	200	1.065	8.68	66.10
	300	0.475	4.30	61.84
	390	0.140	1.58	56.83

magnetic moments. Hence, the difference in the magnetic moment of the [FeO_6], [NiO_6], and [FeO_4] clusters in the $NiFe_2O_4$ and S–$NiFe_2O_4$ samples may be a result of CTAB addition, enhancing the exchange coupling and magnetic response in the as-prepared samples.

In Fig. 5(b and c), the hysteresis loops in a dc magnetic field up to ±3 kOe obtained at different temperatures for each sample (5, 200, 300, and 390 K) revealed a soft ferrimagnetic response. At 5 K, one can observe a large area hysteresis loop in both samples (S–$NiFe_2O_4$ and $NiFe_2O_4$), indicating higher M_r and H_c. The hysteresis area decreases with increasing temperature (200–390 K), indicating superparamagnetism at 390 K [59,60]. All magnetic parameters determined from the hysteresis loops are summarized in Table 3. It is important to keep in mind the effect of chemical composition and crystalline structure in the saturation magnetization (M_s) of NPs [61]. Fig. 5 (d) shows the zero-field cooled (ZFC) and field cooled (FC) plots obtained for samples $NiFe_2O_4$ and S–$NiFe_2O_4$. Both samples exhibit a behavior that is typical for NPs smaller than 50 nm [50]. A peak in the M_{ZFC} plot indicates the blocking temperature (T_B), above which the material becomes paramagnetic [65,66]. Both samples exhibit maximum magnetization at ~390 K, around T_B, which is expected for superparamagnetic materials. Below T_B the material exhibits a ferromagnetic response. Furthermore, ZFC/FC analysis suggests that the Curie temperature (T_{Curie}) for both samples ($NiFe_2O_4$ and S–$NiFe_2O_4$) is higher than 400 K in accordance with the literature ($T_{Curie\ (NiFe2O4)}$ ~ 790–843 K) [61]. The thermal hysteresis below the blocking temperature (T_B) evidenced in the ZFC/FC curves is typical of magnetic NPs. The ZFC/FC plots also reveal that the main differences in the magnetization values found in the curve can be attributed to the higher dispersion of the nanoparticles crystallized in the presence of CTAB, as previously demonstrated by FE-SEM and TEM analyses.

4.4. Biological properties

Fig. 6 shows that the introduction of $NiFe_2O_4$ (1.0, 10.0, and 20.0 μg) reduced the average blood vessel percentage area that remained in the CAM drastically decreased (55.59 ± 5.84, 65.36 ± 3.89, 67.91 ± 10.24, respectively) in comparison with the negative control. A ~50% decrease in angiogenesis was observed for a concentration of 1 μg/mL S–$NiFe_2O_4$, which may be associated with high blood vessel affinity and anti-angiogenic activity, meaning that these NPs effectively concentrate on tumoral vessels, which may enhance drug effectivity and enable simultaneous treatments, image diagnosis of solid tumors, etc. The observed difference is statistically significant ($p < 0.0001$) in the groups treated with nanoparticle dispersions when compared to the control group. Thus, the anti-angiogenic behavior of nickel ferrite NPs is clearly shown, inhibiting angiogenesis in vivo (CAM model), which indicates that future in vivo tests may be very promising.

The results indicate that the size, shape, and magnetic response of NPs contribute to its pharmacokinetic profile. In this work, the anti-angiogenic effect of S–$NiFe_2O_4$ NPs in a chicken embryo model was demonstrated using different concentrations, suggesting the endothelial cells, main targets of anti-angiogenic drugs, effectively internalized the NPs. The S–$NiFe_2O_4$ NPs act via subtle obstructing effects in the chick embryo CAM's microcirculation, inhibiting the vascular endothelial growth factor (VEGF) - induced cell proliferation. S–$NiFe_2O_4$ NPs effectively suppressed neovascularization in the microcirculatory system, induced by VEGF without losing embryo viability, being associated with partial preservation of capillary diameters and connectivity. After the test, CAM structure treated with toxic dosages of NPs appeared to be clustered with a few cellular extensions and vessel formations; hence,

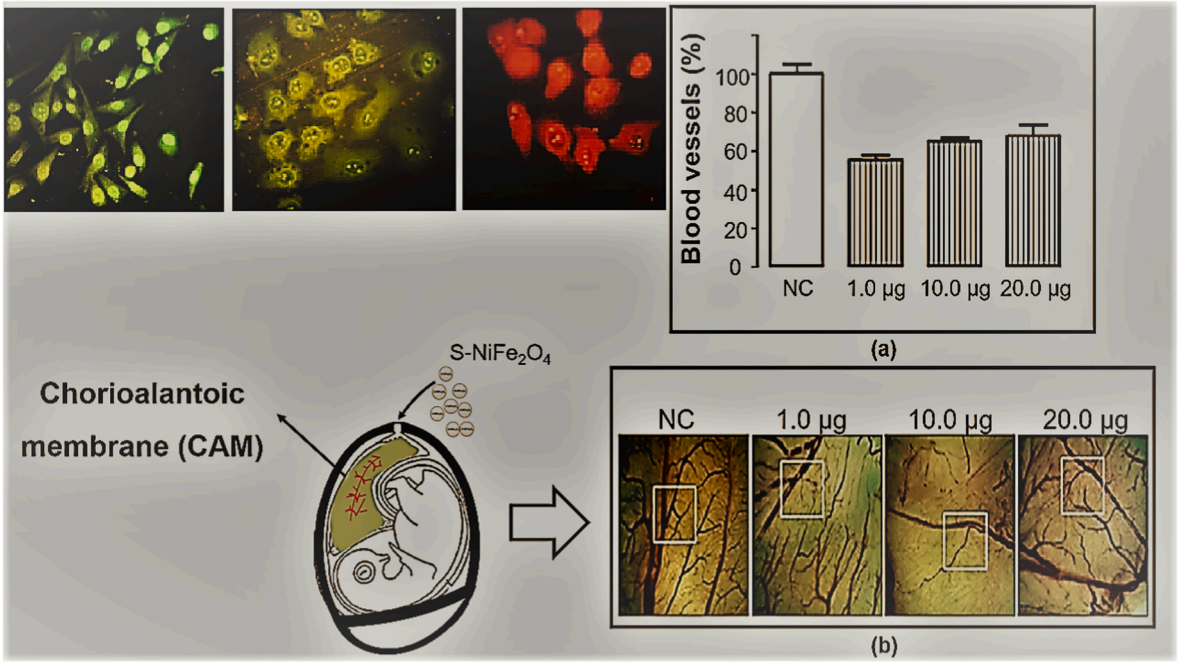

Fig. 6. (a) Effect of treatment with S–$NiFe_2O_4$-NPs (1.0 μg/mL, 10.0 μg/mL and 20.0 μg/mL) on angiogenesis in a chorioallantoic membrane assay and (b) NC: Negative control (saline). The values were calculated by setting the NC to 100%. The columns represent the mean ± SD of the vascularized area (***$p < 0.0001$ in relation to the NC group; ANOVA followed by Bonferroni test; n = 5–10/group).

cell-spreading patterns were restricted compared to the control groups. This may be due to disturbances in the cytoskeletal functions due to NP treatment, suggesting that the S–$NiFe_2O_4$'s anti-angiogenic effect may not be related to any cytotoxic-related effects since there was no significant death of chicken embryos during the experiments.

The literature shows similar results for semiconductor zinc oxide (ZnO) nanoparticles with anti-angiogenic properties [66,67]. The authors demonstrated that ZnO's anti-angiogenic effect depends on concentration and, at low concentrations, ZnO displayed cytotoxic activity against Gram-negative pathogenic bacteria *Pseudomonas aeruginosa*, pathogenic fungus *Candida albicans*, and hepatocarcinoma tumor cells [68–70]. To fully comprehend the anti-angiogenic mechanism in $NiFe_2O_4$, magnetic hyperthermia (MH) treatment could be employed to evaluate the effect on thermo-induced killing *in vitro*, which would help in the development of complementary cancer treatment.

5. Conclusions

In this work, the influence of a surfactant on the order/disorder relationship of the $NiFe_2O_4$ NPs synthesized using the polymeric precursor method was evaluated. S–$NiFe_2O_4$ NPs exhibited a higher-strain structure with less agglomerated, smaller NPs (particle size $\sim$ 28.64 $\pm$ 6.51 nm) in comparison to the $NiFe_2O_4$ sample. The room temperature magnetic response was significantly enhanced on sample S–$NiFe_2O_4$ compared to sample $NiFe_2O_4$, which was associated with changes to the materials' domain structure as a result of particle size decrease. S–$NiFe_2O_4$ NPs displayed dose-dependent effects in the chorioallantoic membrane (CAM). All S–$NiFe_2O_4$ NPs concentrations resulted in vascularization reduction around the solid tumor, contributing significantly to antitumor therapy's effectiveness. Hence, our results indicate the possibility to explore S–$NiFe_2O_4$ NPs as drug delivery agents in targeted cancer therapy. The use of CTAB to synthesize $NiFe_2O_4$ NPs is an effective way to tune the magnetic response of nickel ferrite, making it an interesting alternative to iron oxides (Fe_3O_4 or γ-Fe_2O_3) due to its excellent biocompatibility, high bulk saturation magnetization, and low magnetic anisotropy. The polymeric precursor method is very cost-effective and environmentally friendly through which a single-phase spinel structure can be obtained without generating any toxic by-products. Furthermore, this method can be extended to the synthesis of other spinel ferrite nanoparticles of interest.

Declaration of competing interest

The authors declare that they have no known competing financial interests or personal relationships that could have appeared to influence the work reported in this paper.

Acknowledgments

The authors thank the São Paulo Research Foundation (FAPESP) under CEPID/CDMF, grant ID.:2013/07296-2, and the National Council for Scientific and Technological Development CNPq, grant ID.: 573636/2008-7, for their financial support. We would also like to acknowledge the Arbeitsgruppe at Universität Duisburg-Essen, where the M-H and FZ/ZFC measurements were performed.

Appendix A. Supplementary data

Supplementary data to this article can be found online at https://doi.org/10.1016/j.ceramint.2021.02.191.

References

[1] A. Meidanchi, A. Motamed, Preparation, characterization and in vitro evaluation of magnesium ferrite superparamagnetic nanoparticles as a novel radiosensitizer of breast cancer cells, Ceram. Int. 46 (2020) 17577–17583, https://doi.org/10.1016/j.ceramint.2020.04.057.

[2] M.A. Almessiere, A.V. Trukhanov, F.A. Khan, Y. Slimani, N. Tashkandi, V. A. Turchenko, T.I. Zubar, D.I. Tishkevich, S.V. Trukhanov, L.V. Panina, A. Baykal, Correlation between microstructure parameters and anti-cancer activity of the $[Mn_{0.5}Zn_{0.5}](Eu_xNd_xFe_{2-2x})O_4$ nanoferrites produced by modified sol-gel and ultrasonic methods, Ceram. Int. 46 (2020) 7346–7354, https://doi.org/10.1016/j.ceramint.2019.11.230.

[3] S. Talukdar, R. Rakshit, A. Krämer, F.A. Müller, K. Mandal, Facile surface modification of nickel ferrite nanoparticles for inherent multiple fluorescence and catalytic activities, RSC Adv. 8 (2018) 38–43, https://doi.org/10.1039/c7ra09299g.

[4] U. Kurtan, H. Gungunes, H. Sozeri, A. Baykal, Synthesis and characterization of monodisperse $NiFe_2O_4$ nanoparticles, Ceram. Int. 42 (2016) 7987–7992.

[5] R. Hergt, R. Hiergeist, I. Hilger, W.A. Kaiser, Y. Lapatknikov, S. Margel, U. Richter, Maghemite Nanoparticles with Very High AC-Losses for Application in RF-Magnetic Hyperthermia, 2004, pp. 345–357.

[6] R.R. Koli, N.G. Deshpande, D.S. Kim, A.R. Shelke, A.V. Fulari, V.J. Fulari, H.K. Cho, Tailoring the magnetic hyperthermia performances of gram-bean-extract-mediated highly disperse MFE_2O_4 (M = Fe, Ni, Mn) nanoferrites, Ceram. Int. 46 (2020) 24290–24301.

[7] M. Lickmichand, C.S. Shaji, N. Valarmathi, A.S. Benjamin, R.K. Arun Kumar, S. Nayak, R. Saraswathy, S. Sumathi, N. Arunai Nambi Raj, In vitro biocompatibility and hyperthermia studies on synthesized cobalt ferrite nanoparticles encapsulated with polyethylene glycol for biomedical applications, Mater. Today Proc. 15 (2019) 252–261, https://doi.org/10.1016/j.matpr.2019.05.002.

[8] K. Shimizu, A. Ito, J.K. Lee, T. Yoshida, K. Miwa, H. Ishiguro, Y. Numaguchi, T. Murohara, I. Kodama, H. Honda, Construction of multi-layered cardiomyocyte sheets using magnetite nanoparticles and magnetic force, Biotechnol. Bioeng. 96 (2007) 803–809, https://doi.org/10.1002/bit.21094.

[9] D. Wang, J. He, N. Rosenzweig, Z. Rosenzweig, 2004 - Nano Letters - Superparamagnetic Fe_2O_3 Beads − CdSe ZnS Quantum Dots Core − Shell Nanocomposite Particles for Cell - Wang et.pdf, 2004, pp. 3–7.

[10] S.Z. Mirahmadi-Zare, F. Aboutalebi, M. Allafchian, L. Pirjamali, M.-H. Nasr-Esfahani, Layer by layer coating of NH_2-silicate/polycarboxylic acid polymer saturated by Ni^{2+} onto the super magnetic $NiFe_2O_4$ nanoparticles for sensitive and bio-valuable separation of His-tagged proteins, Protein Expr. Purif. 143 (2018) 71–76.

[11] M. Ahamed, M.J. Akhtar, H.A. Alhadlaq, M.A.M. Khan, S.A. Alrokayan, Comparative cytotoxic response of nickel ferrite nanoparticles in human liver HepG2 and breast MFC-7 cancer cells, Chemosphere 135 (2015) 278–288, https://doi.org/10.1016/j.chemosphere.2015.03.079.

[12] O. Jankovský, V. Rach, D. Sedmidubský, S. Huber, P. Ulbrich, M. Svecová, V. Bartunek, Simple synthesis of free surface nanostructured spinel $NiFe_2O_4$ with a tunable particle size, J. Alloys Compd. 723 (2017) 58–63.

[13] M. Salvati-Niasari, F. Davar, T. Mahmoudi, A simple route to synthesize nanocrystalline nickel ferrite ($NiFe_2O_4$) in the presence of octanoic acid as a surfactant, Polyhedron 28 (2009) 1455–1458.

[14] Y. Slimani, M.A. Almessiere, S. Güner, U. Kurtan, S.E. Shirsath, A. Baykal, I. Ercan, Magnetic and microstructural features of Dy3+ substituted $NiFe_2O_4$ nanoparticles derived by sol–gel approach, J. Sol. Gel Sci. Technol. 95 (2020) 202–210, https://doi.org/10.1007/s10971-020-05292-1.

[15] R. Tiwari, M. De, H.S. Tewari, S.K. Ghoshal, Structural and magnetic properties of tailored $NiFe_2O_4$ nanostructures synthesized using auto-combustion method, Results Phys. 16 (2020) 102916, https://doi.org/10.1016/j.rinp.2019.102916.

[16] M.M. Hessien, N.Y. Mostafa, O.H. Abd-Elkader, Influence of carboxylic acid type on microstructure and magnetic properties of polymeric complex sol-gel driven $NiFe_2O_4$, J. Magn. Magn. Mater. 398 (2016) 109–115.

[17] S. Asiri, M. Sertkol, S. Guner, H. Gungunes, K.M. Batoo, T.A. Saleh, H. Sozeri, M. A. Almessiere, A. Manikandan, A. Baykal, Hydrothermal synthesis of $Co_yZn_yMn_{1-2y}Fe_2O_4$ nanoferrites: magneto-optical investigation, Ceram. Int. 44 (2018) 5751–5759.

[18] K. Seevakan, A. Manikandan, P. Devendran, A. Shameem, T. Alagesan, Microwave combustion synthesis, magneto-optical and electrochemical properties of $NiMoO_4$ nanoparticles for supercapacitor application, Ceram. Int. 44 (2018) 13879–13887.

[19] S. Sagadevan, Z.Z. Chowdhury, R.F. Rafique, Preparation and characterization of nickel ferrite nanoparticles via co-precipitation method, Mater. Res. 21 (2018) 21–25, https://doi.org/10.1590/1980-5373-mr-2016-0533.

[20] M.A. Almessiere, Y. Slimani, S. Guner, M. Nawaz, A. Baykal, F. Aldakheel, A. Sadaqat, I. Ercan, Effect of Nb substitution on magneto-optical properties of $Co_{0.5}Mn_{0.5}Fe_2O_4$ nanoparticles, J. Mol. Struct. 1195 (2019).

[21] M.A. Almessiere, Y. Slimani, U. Kurtan, S. Guner, M. Sertkol, S.E. Shirsath, S. Akhtar, A. Baykal, I. Ercan, Structural, magnetic, optical properties and cation distribution of nanosized $Co_{0.7}Zn_{0.3}Tm_xFe_{2-x}O_4$ ($0.0 \leq x \leq 0.04$) spinel ferrites synthesized by ultrasonic irradiation, Ultrason. Sonochem. 2 (58) (2019) 104638.

[22] A. Sadaqat, M.A. Almessiere, Y. Slimani, S. Guner, M. Sertkol, H. Albertan, A. Baykal, S.E. Shirsath, S.E. Ozcelik, I. Ercan, Structural, optical and magnetic properties of Tb^{3+} substituted Co nanoferrites prepared via sonochemical approach, Ceram. Int. 45 (2019) 22538–22546.

[23] P. Arévalo-Cid, J. Isasi, M. Alcolea Palafox, F. Martín-Hernández, Comparative structural, morphological and magnetic study of MFe2O4 nanopowders prepared by different synthesis routes, Mater, Res. Bull. 123 (2020) 110726, https://doi.org/10.1016/j.materresbull.2019.110726.

[24] A. Omelyanchik, G. Singh, M. Volochaev, A. Sokolov, V. Rodionova, D. Peddis, Tunable magnetic properties of Ni-doped $CoFe_2O_4$ nanoparticles prepared by the sol-gel citrate self-combustion method, J. Magn. Magn. Mater. 476 (2019) 387–391.

[25] T.A. Taha, A.A. Azab, M.A. Sebak, Glycerol-assisted sol-gel synthesis, optical, and magnetic properties of $NiFe_2O_4$ nanoparticles, J. Mol. Struct. 1181 (2019) 14–18.

[26] M. Kumari, M.C. Bhatnagar, Synthesis of nickel ferrite nanorods and nano-octahedrons by hydrothermal method, AIP Conf. Proc. 2220 (2020) 110042, https://doi.org/10.1063/5.0002231.

[27] M. Safaei, H. Beitollahi, M.R. Shishehbore, Synthesis and characterization of $NiFe_2O_4$ nanoparticles using the hydrothermal method as magnetic catalysts for electrochemical detection of norepinephrine in the presence of folic acid, J. Chin. Chem. Soc. 66 (2019) 1597–1603, https://doi.org/10.1002/jccs.201900073.

[28] D.K. Dinkar, B. Das, R. Gopalan, B.S. Dehiya, Effects of surfactant on the structural and magnetic properties of hydrothermally synthesized $NiFe_2O_4$ nanoparticles, Mater. Chem. Phys. 218 (2018) 70–76, https://doi.org/10.1002/bit.21094.

[29] M. Darwish, Q. Sadr Manuchehri, A. Mohammadi, N. Assi, $NiFe_2O_4$ nanomagnets prepared through a microwave autocombustion route as an efficient recoverable adsorbent for 2-nitrophenol removal, Part, Sci. Technol. 37 (2019) 524–533, https://doi.org/10.1080/02726351.2017.1402835.

[30] K. Kombaiah, J.J. Vijaya, L.J. Kennedy, K. Kaviyarasu, Catalytic studies of $NiFe_2O_4$ nanoparticles prepared by conventional and microwave combustion method, Mater. Chem. Phys. 221 (2019) 11–28, https://doi.org/10.1016/j.matchemphys.2018.09.012.

[31] S. Zhao, C. Ge, Z. Yan, J. Zhang, S. Ren, H. Liang, F. Chen, X. Li, One-pot microwave-assisted combustion synthesis of $NiFe_2O_4$-reduced graphene oxide composite for adsorptive desulfurization of diesel fuel, Mater. Chem. Phys. 229 (2019) 294–302.

[32] A. Soto-Arreola, A.M. Huerta-Flores, J.M. Mora-Hernández, L.M. Torres-Martínez, Comparative study of the photocatalytic activity for hydrogen evolution of MFe_2O_4 (M = Cu, Ni) prepared by three different methods, J. Photochem. Photobiol. Chem. 357 (2018) 20–29, https://doi.org/10.1016/j.jphotochem.2018.02.016.

[33] T.V. Tran, U.T.T. Nguyen, T.T. Nguyen, B.N. Hoang, H.T. Tran, N.P.T. Nguyen, V.T. T. Ho, M.T. Nguyen, L.G. Bach, T.D. Nguyen, Synthesis and magnetic properties of graphene oxide-decorated cobalt, manganese and nickel ferrite nanoparticles prepared by polymerized route, IOP Conf. Ser. Mater. Sci. Eng. 479 (2019), https://doi.org/10.1088/1757-899X/479/1/012114, 0–7.

[34] M.L. Martins, A.O. Florentino, A.A. Cavalheiro, R.I.V. Silva, D.I. Dos Santos, M. J. Saeki, Mechanisms of phase formation along the synthesis of Mn-Zn ferrites by the polymeric precursor method, Ceram. Int. 40 (2014) 16023–16031.

[35] N. Choudhary, M.K. Verma, N.D. Sharma, S. Sharma, D. Singh, Superparamagnetic nanosized perovskite oxide $La_{0.5}Sr_{0.5}Ti_{0.5}Fe_{0.5}O_3$ synthesized by modified polymeric precursor method: effect of calcination temperature on structural and magnetic properties, J. Sol. Gel Sci. Technol. 86 (2018) 73–82, https://doi.org/10.1007/s10971-018-4593-2.

[36] R.M. Queiroz, T.L. Coelho, I.M. Queiroz, L.H.O. Pires, I.M.G. Santos, J.R. Zamian, G.N. da Rocha Filho, C.E.F. da Costa, Structural and thermal characterization of $Ni_xZn_{1-x}Al_2O_4$ synthesized by the polymeric precursor method, J. Therm. Anal. Calorim. 124 (2016) 1023–1028, https://doi.org/10.1007/s10973-015-5056-4.

[37] R.F.K. Gunnewiek, C.F. Mendes, R.H.G.A. Kiminami, Synthesis of spinel cobalt oxide nanoparticles using a modified polymeric precursor method, Adv. Powder Technol. 27 (2016) 1056–1061.

[38] C.M. Phan, H.M. Nguyen, Role of capping agent in wet synthesis of nanoparticles, J. Phys. Chem. 121 (2017) 3213–3219, https://doi.org/10.1021/acs.jpca.7b02186.

[39] J.D. Clarke, Cetyltrimethyl ammonium bromide (CTAB) DNA miniprep for plant DNA isolation, Cold Spring Harb. Protoc. 4 (2009) 5177–5179, https://doi.org/10.1101/pdb.prot5177.

[40] A.R. Bucci, L. Marcelino, R.K. Mendes, A. Etchegaray, The antimicrobial and antiadhesion activities of micellar solutions of surfactin, CTAB and CPCl with terpinen-4-ol: applications to control oral pathogens, World J. Microbiol. Biotechnol. 34 (2018) 1–9, https://doi.org/10.1007/s11274-018-2472-1.

[41] J. Folkman, C. Haudenschild, Angiogenesis in vitro, Nature 288 (1980) 551–556.

[42] H.M. Rietveld, A profile refinement method for nuclear and magnetic structures, J. Appl. Crystallogr. 2 (1969) 65–71, https://doi.org/10.1107/s0021889869006558.

[43] A.A. Coelho, TOPAS and TOPAS-Academic: an optimization program integrating computer algebra and crystallographic objects written in C++, J. Appl. Crystallogr. 51 (2018) 210–218, https://doi.org/10.1107/S1600576718000183.

[44] A. Bertran, S. Sandoval, J. Oró-Solé, À. Sánchez, G. Tobias, Particle size determination from magnetization curves in reduced graphene oxide decorated with monodispersed superparamagnetic iron oxide nanoparticles, J. Colloid Interface Sci. 566 (2020) 107–119, https://doi.org/10.1016/J.JCIS.2020.01.072.

[45] A.C. Sparavigna, On the use of ImageJ segmentation, Zenodo Repos (2020) 1–11, https://doi.org/10.5281/zenodo.3629411.

[46] P. Dorenbos, A review on how lanthanide impurity levels change with chemistry and structure of inorganic compounds, ECS J. Solid State Sci. Technol. 2 (2013) R3001–R3011, https://doi.org/10.1149/2.001302jss.

[47] K.N. Subramanyam, Neutron and X-ray diffraction studies of certain doped nickel ferrites, J. Phys. C Solid State Phys. 4 (1971) 2266–2268, https://doi.org/10.1088/0022-3719/4/15/012.

[48] L.B. Mccusker, R.B. Von Dreele, D.E. Cox, D. Louër, P. Scardi, Rietveld refinement guidelines, J. Appl. Crystallogr. 32 (1999) 36–50, https://doi.org/10.1107/S0021889898009856.

[49] H.L. Andersen, M. Saura-Múzquiz, C. Granados-Miralles, E. Canévet, N. Lock, M. Christensen, Crystalline and magnetic structure-property relationship in spinel ferrite nanoparticles, Nanoscale 10 (2018) 14902–14914, https://doi.org/10.1039/c8nr01534a.

[50] A.V. Humbe, J.S. Kounsalye, M.V. Shisode, K.M. Jadhav, Rietveld refinement, morphology and superparamagnetism of nanocrystalline Ni0.70-xCuxZn0.30Fe2O4 spinel ferrite, Ceram. Int. 44 (2018) 5466–5472.

[51] V. Šepelák, A. Buchal, K. Tkácová, K.D. Becker, Nanocrystalline structure of the metastable ball-milled inverse spinel-ferrites, Mater. Sci. Forum. 278–281 (1998) 862–867.

[52] A. Ahlawat, V.G. Sathe, V.R. Reddy, A. Gupta, Mossbauer, Raman and X-ray diffraction studies of superparamagnetic $NiFe_2O_4$ nanoparticles prepared by solgel auto-combustion method, J. Magn. Magn. Mater. 323 (2011) 2049–2054, https://doi.org/10.1016/j.jmmm.2011.03.017.

[53] M. Maria Lumina Sonia, S. Anand, S. Blessi, S. Pauline, A. Manikandan, Effect of surfactants (PVB/EDTA/CTAB) assisted sol-gel synthesis on structural, magnetic and dielectric properties of $NiFe_2O_4$ nanoparticles, Ceram. Int. 44 (2018) 22068–22079, https://doi.org/10.1016/j.ceramint.2018.08.317.

[54] A.B. Mapossa, J. Dantas, M.R. Silva, R.H.G.A. Kiminami, A.C.F.M. Costa, M. O. Daramola, Catalytic performance of $NiFe_2O_4$ and $Ni_{0.3}Zn_{0.7}Fe_2O_4$ magnetic nanoparticles during biodiesel production, Arab. J. Chem. 13 (2020) 4462–4476, https://doi.org/10.1016/j.arabjc.2019.09.003.

[55] Rahil Abbasi Hormozi, H. Tavakkoli, A.R. Shabari, M. Nikpour, Facile synthesis and characterization of nanospinel ferrites: structural, magnetic, and optical studies, Russ. J. Inorg. Chem. 65 (2020) 1093–1101, https://doi.org/10.1134/S0036023620070104.

[56] L.I. Granone, A.C. Ulpe, L. Robben, S. Klimke, M. Jahns, F. Renz, T.M. Gesing, T. Bredow, R. Dillert, D.W. Bahnemann, Effect of the degree of inversion on optical properties of spinel $ZnFe_2O_4$, Phys. Chem. Chem. Phys. 20 (2018) 28267–28278, https://doi.org/10.1039/c8cp05061a.

[57] A. Ahlawat, V.G. Sathe, Raman study of $NiFe_2O_4$ nanoparticles, bulk and films: effect of laser power, J. Raman Spectrosc. 42 (2011) 1087–1094, https://doi.org/10.1002/jrs.2791.

[58] J.C. Howard, J.D. Enyard, G.S. Tschumper, Assessing the accuracy of some popular DFT methods for computing harmonic vibrational frequencies of water clusters, J. Chem. Phys. 143 (2015), https://doi.org/10.1063/1.4936654.

[59] M.J. Livani, M. Ghorbani, H. Mehdipour, Preparation of an activated carbon from hazelnut shells and its hybrids with magnetic $NiFe_2O_4$ nanoparticles, N. Carbon Mater. 33 (2018) 578–586, https://doi.org/10.1016/s1872-5805(18)60358-0.

[60] S. Das, M. Bouodina, C. Manoharan, The influence of cationic surfactant CTAB on optical, dielectric and magnetic properties of cobalt ferrite nanoparticles, Ceram. Int. 46 (2020) 11705–11716, https://doi.org/10.1016/j.ceramint.2020.10.144.

[61] U. Klekotka, D. Satuła, A. Basa, B.K. Szostko, Importance of surfactant quantity and quality on growth regime of iron oxide nanoparticles, Materials 13 (2020) 1747–1759, https://doi.org/10.3390/ma13071747.

[62] H. Hu, Z. Tian, J. Liang, H. Yang, A. Dai, L. An, H. Wu, S. Yang, Surfactant-controlled morphology and magnetic property of manganese ferrite nanocrystal contrast agent, Nanotechnology 22 (2011), 085707-085714.

[63] Y.L. Raikher, V.I. Stepanov, J. Depeyrot, M.H. Sousa, F.A. Tourinho, E. Hasmonay, R. Perzynski, Dynamic optical probing of the magnetic anisotropy of nickel-ferrite nanoparticles, J. Appl. Phys. 96 (2004) 5226–5233, https://doi.org/10.1063/1.1790574.

[64] M. Vadivel, R.R. Babu, K. Ramamurthi, M. Arivanandhan, CTAB cationic surfactant assisted synthesis of $CoFe_2O_4$ magnetic nanoparticles, Ceram. Int. 42 (2016) 19320–19328, https://doi.org/10.1016/j.ceramint.2016.09.101.

[65] A.-H. Foulani, A. Aamouche, F. Mohseni, J.S. Amaral, D.M. Tobaldi, R.C. Pullar, Effect of surfactants on the optical and magnetic properties of cobalt-zinc ferrite $Co_{0.5}Zn_{0.5}Fe_2O_4$, J. Alloys Compd. 774 (2019) 1250–1259, https://doi.org/10.1016/j.jallcom.2018.09.393.

[66] G. Nabiyouni, M.J. Fesharaki, M. Mozafari, J. Amighian, Characterization and magnetic properties of nickel ferrite nanoparticles prepared by ball milling technique, Chin. Phys. Lett. 27 (2010), https://doi.org/10.1088/0256-307X/27/12/126401.

[67] M.A. Almessiere, Y. Slimani, H. Gungunes, S. Ali, A. Manikandan, I. Ercan, A. Baykal, A.V. Trukhanov, MAgnetic attributes of $NiFe_2O_4$ nanoparticles: influence of dysprosium ions (Dy3+) substitution, Nanomaterials 820 (2019) 1–15, https://doi.org/10.3390/nano9060820.

[68] M. Divya, B. Vaseeharan, M. Abinaya, S. Vijayakumar, M. Govindarajan, N. S. Alharbi, S. Kadaikunnan, J.M. Khaled, G. Benelli, Biopolymer gelatin-coated zinc oxidenanoparticles showed high antibacterial, antibiofilm and anti-angiogenic activity, J. Photochem. Photobiol. B: Biol. 178 (2018) 211–218, https://doi.org/10.1016/j.jphotobiol.2017.11.008.

[69] S. Sindhwani, A.M. Syed, J. Ngai, B.R. Kingston, L. Maiorino, J. Rothschild, P. MacMillan, Y. Zhang, N.U. Rajesh, T. Hoang, et al., The entry of nanoparticlesinto solid tumours, Nat. Mater. 19 (2020) 566–575, https://doi.org/10.1038/s41563-019- 0566-2.

[70] S. Wilhelm, A.J. Tavares, Q. Dai, S. Ohta, J. Audet, H.F. Dvorak, W.C.W. Chan, Analysis of nanoparticle delivery to tumours, Nat. Rev. Mater. (2016), https://doi.org/10.1038/natrevmats.2016.14.